Cation-Exchange-Derived $Cu_{1.8}S$-$Fe_{0.8}S$ Nanocomposites for the Construction of a Photothermal Immunoplatform toward Sensitive Alpha-Fetoprotein Assay

Chenxin Tian,[a] *Zengrong Fang,*[a] *Mingzhe Jiang,*[b] *Min Wang,*[a*] *Chenglin Hong,*[b*] *Qingwang Xue*[a*]

[a]*Department of Chemistry, Liaocheng University, Liaocheng, 252059, Shandong, China.*

[b]*State Key Laboratory Incubation Base for Green Processing of Chemical Engineering, Engineering Research Center of Materials-Oriented Chemical Engineering of Xinjiang Production and Construction Corps, School of Chemistry and Chemical Engineering, Shihezi University, Shihezi 832003, PR China.*

*Corresponding author:

Email: wangm@lcu.edu.cn;
hcl_tea@shzu.edu.cn;
xueqingwang1983@163.com.

2 Experimental section

2.1 Reagents and Chemicals

Octadecene (ODE), oleamide (OLAM), tri-octylphosphine (TOP), and tert-dodecathiole (t-DDT) were all supplied by Aladdin (Shanghai, China). Copper(II) chloride ($CuCl_2$), iron(III) chloride ($FeCl_3$), isopropanol, and n-hexane were all supplied by McLean (Shanghai, China). Bovine serum albumin (BSA) was supplied by Alpha Aesa (Tianjin, China). Bovine serum albumin (BSA) was supplied by Alpha Aesa (Tianjin, China). AFP antigen and antibody were supplied by Bosai Biotechnology (Zhengzhou, China).

Freeze dryer (LGJ-10) (Beijing Sihuan Scientific Instrument Factory Co., Ltd.), 3D Printers（Shenzhen Aurora a8），Scanning electron microscopy (SEM) (JEOLJSM-6700F, Hitachi, Japan), Transmission electron microscopy was performed on an H600TEM (Hitachi, Tokyo, Japan), Fourier Transform Infrared Spectroscopy (FTIR) (IRsolution, Shimadzu，Japan), X-ray diffractometer (XRD) (D8 Advance, Bruker AG), XPS on a Thermo Scientific K-Alpha+ photoelectron spectrometer (VG Co.), in which monochromatic Al Kα X-ray radiation was used as the X-ray source for excitation, Three-electrode Electrochemical Workstation (Chi-760E, Shanghai, China).

2.2 Preparation of $Cu_{1.8}S$ NPLs

The material was synthesized following the protocols described in the literature, with modifications based on practical considerations[1]. The procedure primarily involved mixing $CuCl_2$ (1.5 mmol), OLAM (2.5 mL), and ODE (15 mL) in a three-neck round-bottom flask, evacuating the flask for 10 min, and then purging with N_2. Subsequently, the flask was heated. Upon reaching 80 °C, the system was evacuated for 10 min and purged with N_2. Under a continuous N_2 purge, the temperature was further raised to 180 °C and maintained for 5 min. At 120 °C, t-DDT (6 mL) was rapidly added to the system. Finally, the mixture was cooled to room temperature in a water bath, centrifuged at

9000 rpm, and washed with a mixture of acetone and isopropanol (V:V = 1:1). The resulting NPLs were dispersed in n-hexane and dried under vacuum for later use.

2.3 Preparation of $Cu_{1.8}S$-$Fe_{0.8}S$ NPLs

Add $FeCl_3$ (0.4 mmol), OLAM (4 mL), and ODE (10 mL) to a three-neck round-bottom flask, evacuate under vacuum for 10 min, and then purge with N_2. Upon heating to 80 °C, evacuate under vacuum again for 10 min, and continue heating to 180 °C while purging with N_2. Hold at this temperature for 30 min to form a homogeneous Fe-OLAM complex solution, then cool to 100 °C and set aside.

$Cu_{1.8}S$ NPLs (0.4 mmol) were dispersed in a TOP solution, followed by ultrasonication and vacuum degassing for 30 min to obtain a well-dispersed $Cu_{1.8}S$ NPLs/TOP suspension. The suspension was rapidly injected into a Fe-OLAM complex solution at 100 °C. The reaction was allowed to proceed for 5 min, then cooled to room temperature. The mixture was centrifuged and washed three times with a hexane/isopropanol mixture (V:V = 1:1), dispersed in hexane, and vacuum-dried for later use.

Following the steps described above, we synthesized products with different molar ratios to investigate cation exchange behavior. The specific ratios were: $[FeCl_3]/[CuCl_2] = 0.25, 0.5, 1, 2$, and 4.

2.4 Preparation of the Ab_2-Label: Ab_2-$Cu_{1.8}S$-$Fe_{0.8}S$ NPLs

As shown in Scheme 1(A), firstly, 400 μL of EDC/NHS (0.1 M, volume ratio 1:4) was added to 2 mL of $Cu_{1.8}S$-$Fe_{0.8}S$ NPLs solution (0.5 mg/mL) to activate the amino groups on the material, followed by the addition of 2 mL of Ab2 (AFP secondary antibody). After stirring the mixture at 4 °C for 12 h, add 1200 μL of BSA (bovine serum albumin) to block non-specific binding sites. After 2 h, the product was collected by centrifugation at low temperature, redispersed in 2 mL of deionized water, and stored at 4 °C for further use.

2.5 Development of a Photothermal Immunotherapy Platform

As shown in Scheme 1(B), add 50 µL of Ab_1 (AFP primary antibody, 9.36 µg/mL), BSA (1 wt%), and AFP antigen at various concentrations sequentially to a 96-well plate for incubation during the immunoreaction. The incubation times are 1 h, 40 min, and 35 min, respectively. After the immunoreaction is complete, add 50 µL of Ab_2-Label for biomolecular conjugation, and begin temperature-dependent signal acquisition after 1 h. It is important to note that the well must be washed with deionized water after each incubation step.

2.6 Test Methods

Place the incubated 96-well plate onto the sample holder of the 3D-printed device, then slide the sample holder into the three-way cavity of the main unit. Turn on the laser emitter, adjust it to the desired power, and, following the test sequence, slide the sample holder one by one beneath the light source. Turn on the near-infrared light emitter. The near-infrared light is emitted by the laser emitter, transmitted through an optical fiber to the laser probe, and directed onto the surface of the test sample, causing its temperature to change. Temperature signals are captured using a smartphone connected to a near-infrared camera. The near-infrared camera is ingeniously mounted inside the 3D-printed device and connected to the smartphone via a Type-C port. The smartphone then identifies the temperature signals, captures images for record-keeping, and performs comparative analysis, thereby enabling portable, visual, and low-cost detection of the target object.

All experiments involving human blood samples were performed in compliance with the institutional guidelines and relevant national regulations in China. The study was approved by the Ethics Committee of Liaocheng University. Informed consent was obtained from all individual participants prior to sample collection.

3 Results and discussion

3.1 Material characterization

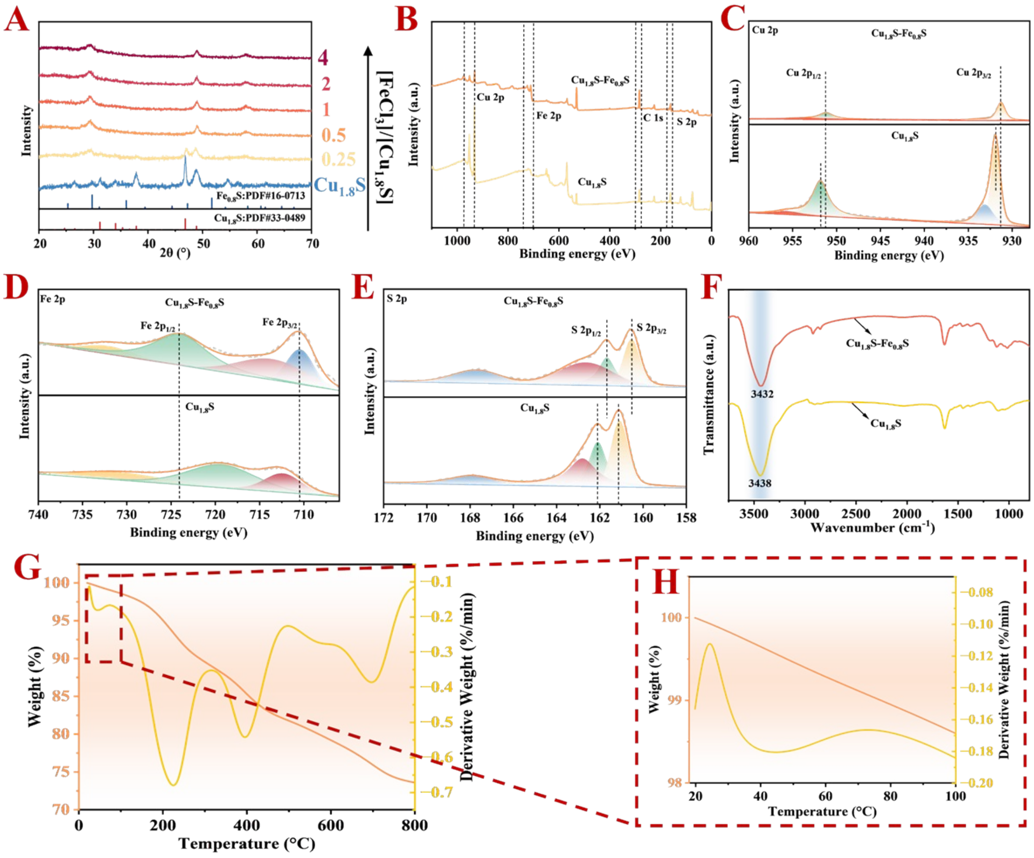

Figure S1. (A) XRD of $Cu_{1.8}S$ and CE exchange products with different ratios; (B) XPS spectra and high resolution of $Cu_{1.8}S$-$Fe_{0.8}S$: Cu（C）； Fe（D）； S（E）; (F) FT-IR testing of $Cu_{1.8}S$-$Fe_{0.8}S$; Thermal stability analysis of (G-H) $Cu_{1.8}S$-$Fe_{0.8}S$.

3.2 Investigation of the Formation Process of $Cu_{1.8}S$-$Fe_{0.8}S$ NPLs

To better understand the CE reaction process, we carefully monitored the morphological evolution of the material by characterizing an intermediate product formed during part of the CE reaction ($[FeCl_3]/[Cu_{1.8}S]=0.5$). EDS results confirmed the time-dependent change in the composition of the products during the CE reaction (**Figure S2** (G, H)), with the iron content increasing continuously as the reaction progressed. The HRTEM images in **Figure S2** (A-C) reveal the shape transformation from hexagonal $Cu_{1.8}S$ NPLs to $Cu_{1.8}S$-$Fe_{0.8}S$ NPLs within just 5 min. Specifically, the NPLs have a large basal area. After 30 s of the reaction, the material's surface partially begins to thin and ablate, nearly forming voids, as shown in **Figure S2** (A). As the reaction continued, the thin-layer regions expanded at 3 min, forming a varying number of compartments (**Figure S2** (B)). Finally, at 5 min, due to the limited supply of iron ions, hexagons of varying thickness formed, with the overall size remaining nearly unchanged (**Figure S2** (C)). Mapping tests revealed the specific distribution of Cu and Fe throughout the process. As shown in **Figure S2** (D-F), at the beginning of 30 s, Cu was distributed throughout the entire area, while Fe was concentrated in a small part of the NPLs. As the reaction proceeded, the copper layer became thinner, and iron was mainly located in the thin layer of the thick copper part. The significant distribution of light and dark areas in the figure indicates the presence of two phases on the NPLs [2] .

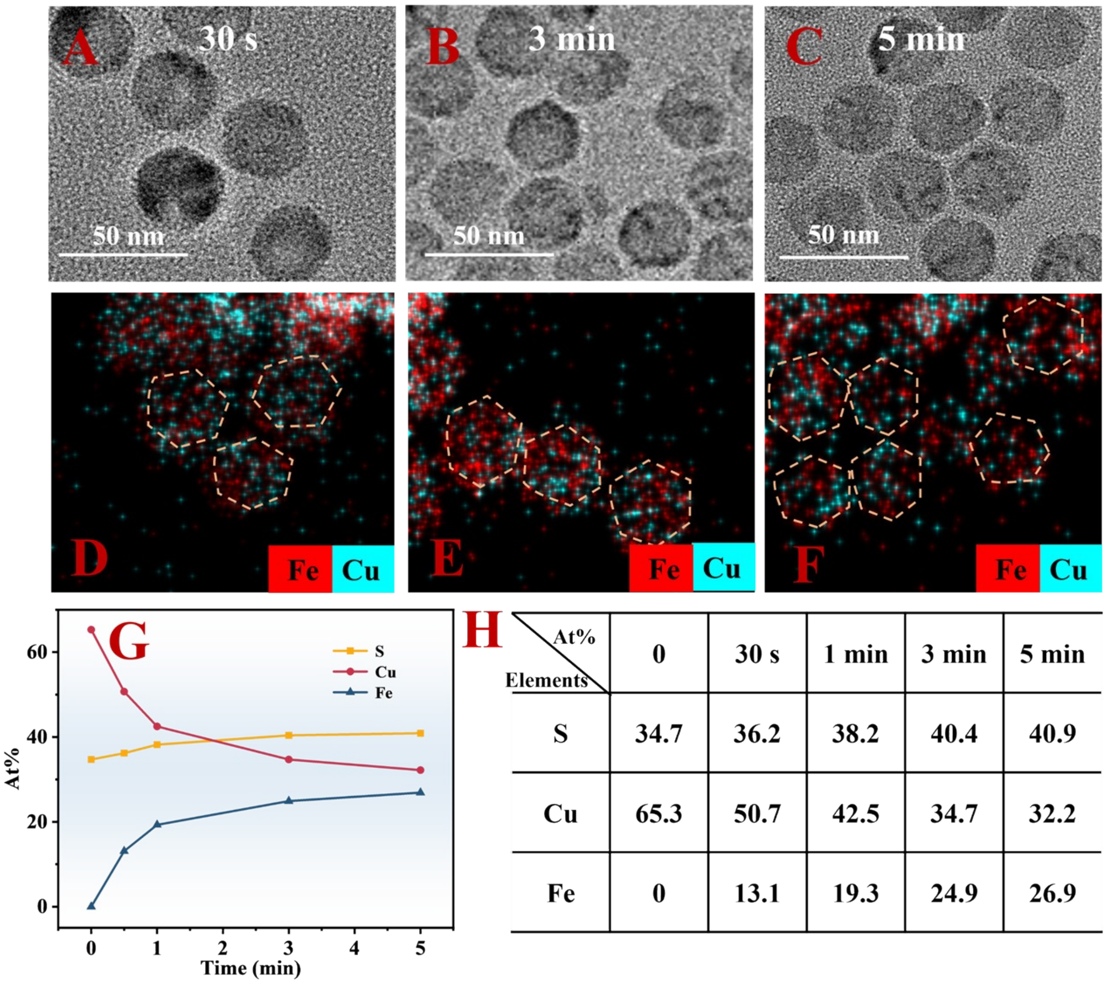

At% / Elements	0	30 s	1 min	3 min	5 min
S	34.7	36.2	38.2	40.4	40.9
Cu	65.3	50.7	42.5	34.7	32.2
Fe	0	13.1	19.3	24.9	26.9

Figure S2. HRTEM and mapping images of CE reaction at 30 s (A, D); 3 min (B, E) and 5 min (C, F); (G, H) EDX and specific contents of the material at different reaction time periods: $[FeCl_3]/[Cu_{1.8}S]=0.5$

To further investigate the CE formation process, we continued to increase the Fe^{3+} dosage. An additional Fe-OLAM suspension with a molar ratio of $[FeCl_3]/[Cu_{1.8}S]=2$ was added to the reaction solution of the aforementioned $Cu_{1.8}S$-$Fe_{0.8}S$ HNPLs ($[FeCl_3]/[Cu_{1.8}S$-$Fe_{0.8}S] = 0.5$), and the products were identified at different reaction times (**Figure S3** (G, H)). The reaction restarted immediately after the additional Fe^{3+} injection, and EDS spectra showed that the Fe^{3+} content in the material gradually increased as the reaction proceeded. The HRTEM images also clearly reveal the changes in the products at different stages of the exchange time, as the supply of a large amount of Fe^{3+} allowed the previously formed voids to be repaired. After 5 min of reaction, the Cu content dropped to a minimum, resulting in $Cu_{1.8}S$-$Fe_{0.8}S$ NPLs of uniform size (**Figure S3** (A-F)).

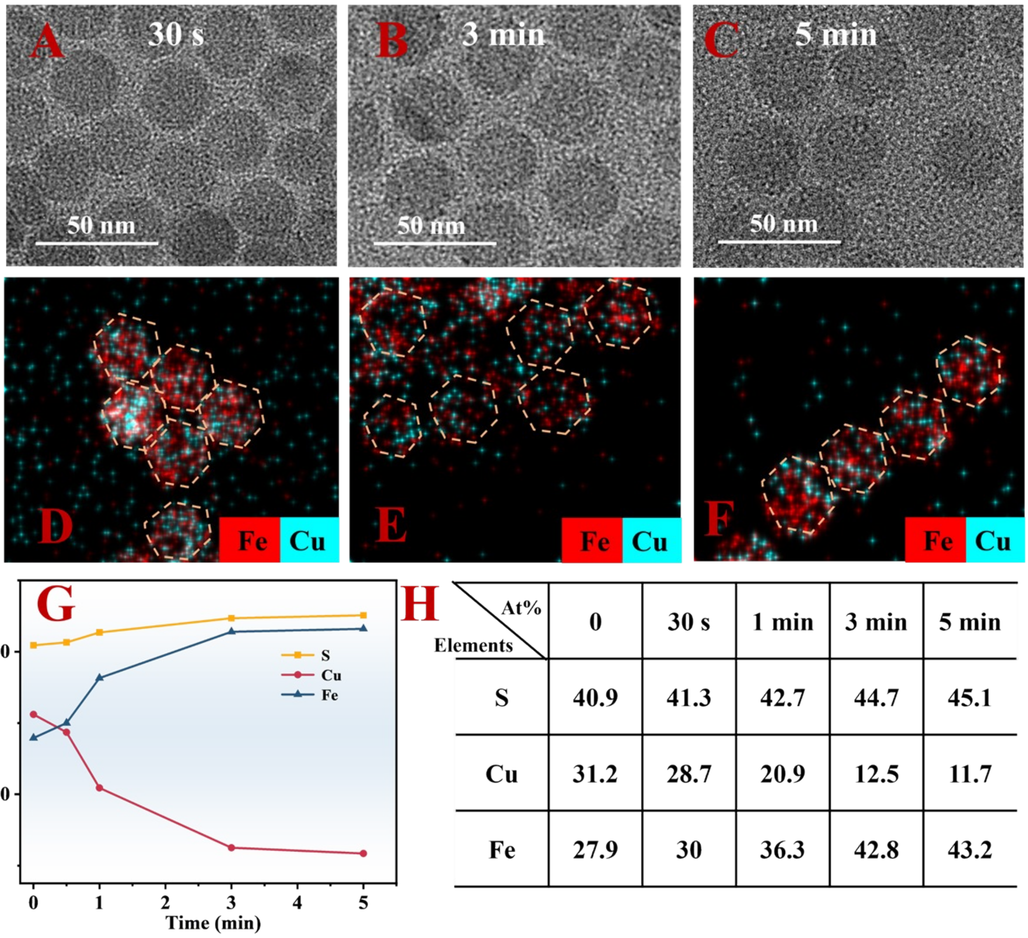

At% / Elements	0	30 s	1 min	3 min	5 min
S	40.9	41.3	42.7	44.7	45.1
Cu	31.2	28.7	20.9	12.5	11.7
Fe	27.9	30	36.3	42.8	43.2

Figure S3. HRTEM and mapping images of CE reaction at 30 s (A, D); 3 min (B, E) and 5 min (C, F); (G, H) EDX and specific contents of the material at different reaction time periods: $[FeCl_3]/[Cu_{1.8}S] = 4$.

It is worth noting that the formation of $Fe_{0.8}S$ in the material stems partly from the exchange of Fe and Cu during the CE process, and partly from the combination of Fe ions with dissolved S^{2-} in the solution, leading to its deposition on $Cu_{1.8}S$ and the formation of $Cu_{1.8}S$-$Fe_{0.8}S$ HNPLs. X-ray fluorescence (XRF) spectroscopy revealed that the supernatant contained a relatively high concentration of S during the cavity formation process, indicating that $Cu_{1.8}S$ partially dissolved during certain stages of the CE process. When the cavities were repaired, the amount of S decreased (**Figure S4**).

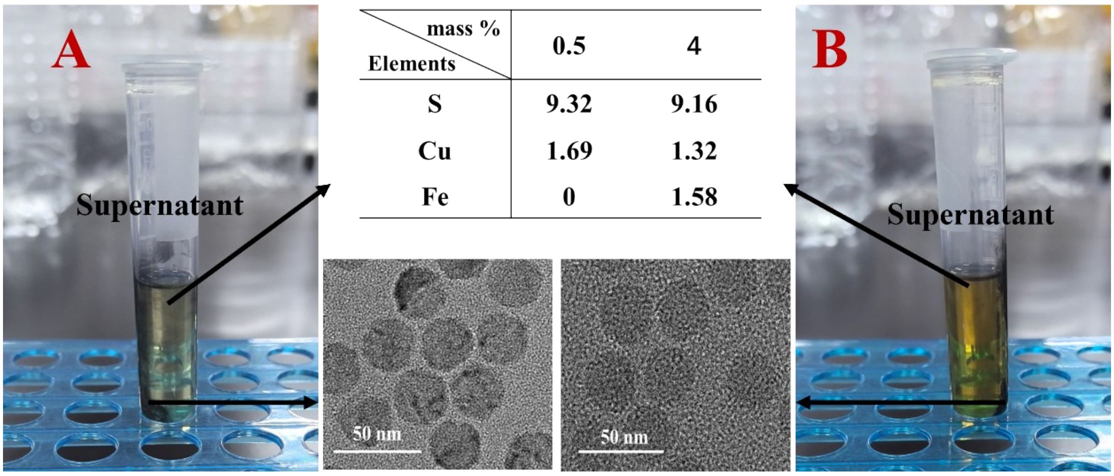

mass % / Elements	0.5	4
S	9.32	9.16
Cu	1.69	1.32
Fe	0	1.58

Figure S4. XRF test results of $Cu_{1.8}S$-$Fe_{0.8}S$ HNPLs: (A) $[FeCl_3]/[Cu_{1.8}S] = 0.5$; (B) $[FeCl_3]/[Cu_{1.8}S]=4$.

Based on the abovementioned characteristics, we have proposed a conversion mechanism for the entire reaction. The formation of NPLs with a hollow structure in the early stages most likely results from the CE of Fe and Cu, primarily triggered by anisotropic ion migration within individual NPLs. Starting from random locations on the NPLs, these events serve as the initiation points for subsequent anisotropic CE, ultimately leading to the formation of heterojunction structures[3, 4]. As demonstrated in our experiments, the CE between $Cu_{1.8}S$ NPLs and Fe^{3+} initiates at specific sites on the NPLs, Subsequently, the unequal rates of outward diffusion of the host Cu^{2+} and inward diffusion of the guest Fe^{3+} result in the formation of varying numbers of voids on the hexagonal nanosheets. This reaction, triggered by the significant disparity in the outward and inward migration rates of the cations, is commonly interpreted as the nanoscale Kirkendall effect[5, 6]. Furthermore, the formation based on this effect have been reported in numerous studies. This morphological change in the material, resulting from the imbalance in the migration rates of the host and guest cations, provides a universal method for the controlled synthesis of targeted nanoheterostructures[7].

3.3 Investigation of the Photothermal Mechanism of $Cu_{1.8}S$-$Fe_{0.8}S$ NPLs

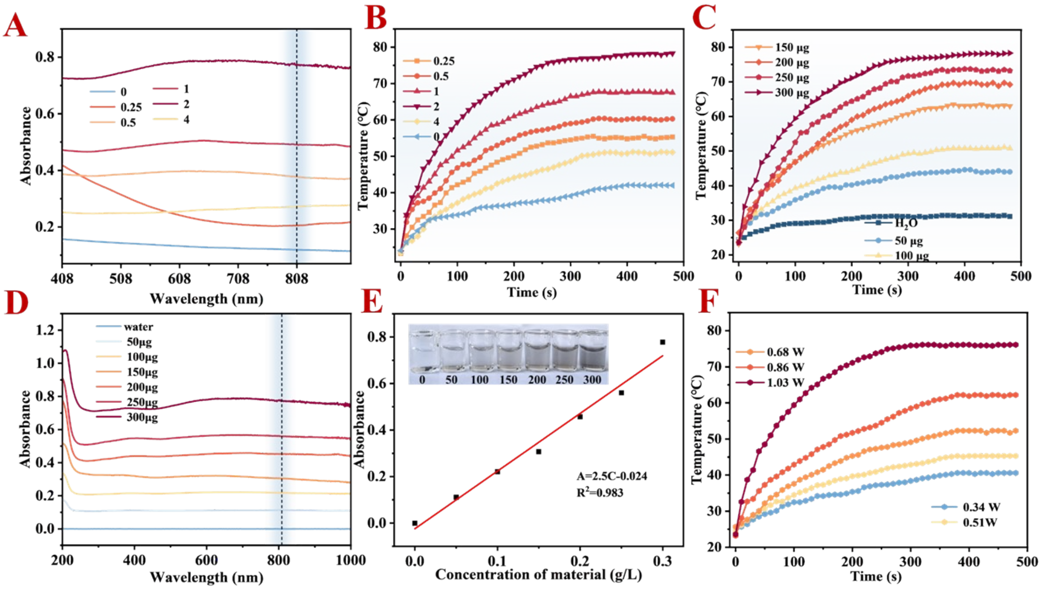

Figure S5. UV-vis-NIR (A) and temperature rise conditions (B) of $[FeCl_3]/[Cu_{1.8}S]$ with different ratios; Temperature rise conditions(C) and UV-vis-NIR (D) of water and $Cu_{1.8}S$-$Fe_{0.8}S$ NPLs with different concentrations; (E) Linear relationship of ultraviolet absorbance of materials with different concentrations; (F) power and temperature rise conditions.

The photothermal stability was determined based on the temperature changes of $Cu_{1.8}S$-$Fe_{0.8}S$ NPLs (300 μg/mL), and the heating behavior was compared with that of the original material, $Cu_{1.8}S$, at the same concentration. Under irradiation by an 808 nm laser, the maximum temperature showed only slight variation during four laser on/off cycles, demonstrating the material’s excellent thermal stability. At the same time, a comparison revealed that after CE the temperature variation was significant, as shown in **Figure S6**(A). **Figures S6**(B, C) show the cooling curves for the $Cu_{1.8}S$-$Fe_{0.8}S$ NPLs and $Cu_{1.8}S$ NPLs, respectively.

The photothermal conversion efficiency of NPLs was calculated based on the literature[8, 9]. The specific calculation formula is as follows. The energy balance of this system is:

$$\sum_i m_i C_{p,i} \frac{dT}{dt} = Q_{NPs} + Q_s - Q_{loss} \tag{1}$$

where m and C_p are the mass and heat capacity, respectively, the suffix " i " for m and C_p denote the solvent (water) or dispersed material (nanoparticles), T is the solution temperature. Q_{NPs} is the photothermal energy absorbed per second by the NPLs:

$$Q_{NPs} = I\left(1 - 10^{-A_\lambda}\right)\eta \tag{2}$$

where I is the laser power; A_λ is the absorbance of the aqueous solution of NPLs at 808 nm; η is the photothermal conversion efficiency of NPLs the conversion efficiency of the absorbed light energy into heat energy, Q_{loss} is the heat lost to the environment:

$$Q_{loss} = hA\Delta T \tag{3}$$

where h is the heat transfer coefficient; A is the surface area of the vessel; and ΔT is the change in temperature (T-T_{sur}, the difference between the solution temperature and the ambient temperature).

Q_S is the heat associated with the light absorption of the solvent, where heat input equals heat output at the highest steady state temperature:

$$Q_S = Q_{loss} = hA\Delta T_{max,H_2O} \tag{4}$$

where $\Delta T_{max,H_2O}$ is the temperature change at the maximum steady state temperature.

In the NPLs solution system, where the heat input is two parts, the heat generated by the nanoparticles (QNPs) and the heat generated by the solvent water (QS):

$$Q_{NPs} + Q_S = Q_{loss} = hA\Delta T_{max,mix} \tag{5}$$

where $\Delta T_{max,mix}$ is the value of temperature change of NPLs dispersion at the highest steady state temperature. According to Eq (2), (4) and (5) the photothermal conversion efficiency can be obtained as follows:

$$\eta = \frac{hA(\Delta T_{max,mix} - \Delta T_{max,H_2O})}{I(1 - 10^{-A_\lambda})} \tag{6}$$

To find the value of *hA*, we introduce *θ* and define it as the ratio of ΔT and ΔT_{max}:

$$\theta = \frac{\Delta T}{\Delta T_{max}} \tag{7}$$

Bringing Eq (7) into equation Eq (1):

$$\frac{d\theta}{dt} = \frac{hA}{\sum_i m_i C_{p,i}} \left[\frac{Q_{NPs} + Q_S}{hA\Delta T_{max}} - \theta \right] \tag{8}$$

When the laser is turned off, $Q_{NPs} + Q_S = 0$ is carried over into Eq (8):

$$dt = -\frac{\sum_i m_i C_{p,i}}{hA} \frac{d\theta}{\theta} \tag{9}$$

$$t = -\frac{\sum_i m_i C_{p,i}}{hA} ln\theta \tag{10}$$

where $\frac{\sum_i m_i C_{p,i}}{hA}$ can be obtained by calculating the linear relationship between the time of the cooling curve of NPLs and -ln(θ), The m_{NPs} and $C_{p,NPs}$ of the nanomaterials were neglected. m_{H_2O} is 3×10^{-4} kg, and C_{p,H_2O} is 4.2×10^{3} J/kg·°C. Consequently, *hA* is 0.00638 and 0.00427, respectively. Finally, the photothermal conversion efficiency is calculated by Eq. (6). $\Delta T_{max,mix}$ is 54.7 and 19.5 °C, respectively, while $\Delta T_{max,H_2O}$ is 6.7 °C. The power density I is 2.05 W/cm², and A_λ is 0.77 and 0.082, respectively. The final

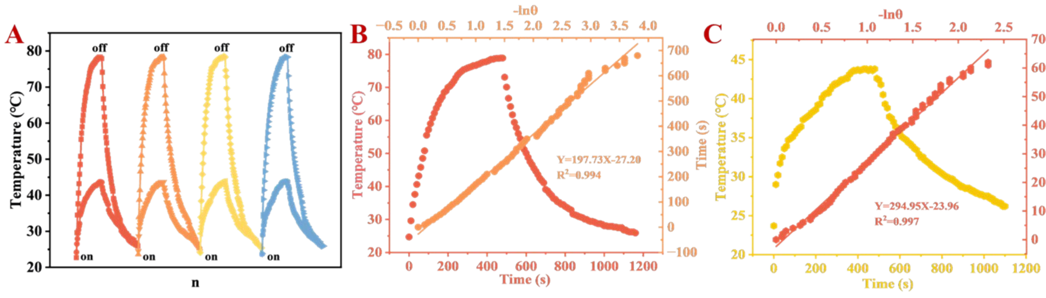

calculated values for η are 18.0% and 15.4%, respectively.

Figure S6. (A) Thermal stability testing; Cooling curve of material: (B) $Cu_{1.8}S$-$Fe_{0.8}S$ NPLs; (C) $Cu_{1.8}S$.

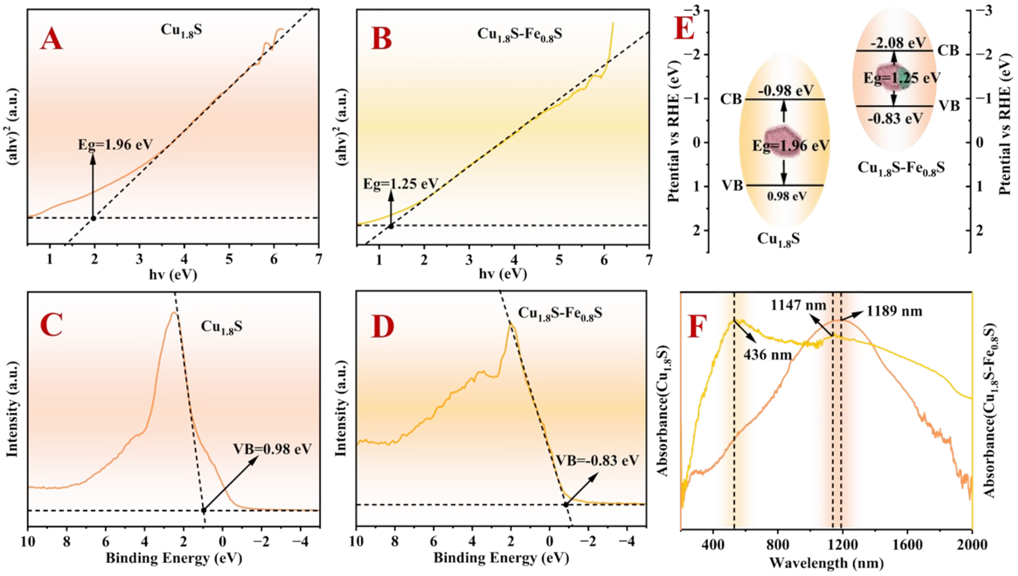

Figure S7. Band gap test results: (A)$Cu_{1.8}S$ and (B)$Cu_{1.8}S$-$Fe_{0.8}S$ NPLs; Price band test results: $Cu_{1.8}S$ (C) and $Cu_{1.8}S$-$Fe_{0.8}S$ NPLs (D); (E) Bandgap diagram; (C) UV diffuse reflectance testing of $Cu_{1.8}S$-$Fe_{0.8}S$ NPLs

When semiconductor materials are excited by photons with sufficient energy, electrons are promoted to excited states. These excited states are energy-surplus and unstable, requiring a de-excitation process. Suppressing radiative emission (fluorescence) during de-excitation represents another effective strategy to enhance photothermal conversion and this interpretation is also applicable to our materials. We compared the Stokes shifts before and after the CE reaction and found that the Stokes shift was significantly enlarged after Fe^{3+} exchange (**Figures S8A, B**). Meanwhile, the emission intensity decreased accompanied by pronounced fluorescence quenching, as shown in **Figure S8C**, which constitutes one of the reasons for the enhanced photothermal conversion efficiency of $Cu_{1.8}S$-$Fe_{0.8}S$ NPLs. Based on the above results, the strong photothermal effect and excellent photothermal stability demonstrate that $Cu_{1.8}S$-$Fe_{0.8}S$ NPLs possess promising application potential in photothermal immunoassays and can be employed in such assays. The actual temperature-rise profiles for photothermal conversion of different materials are presented in **Figure**

S8D.

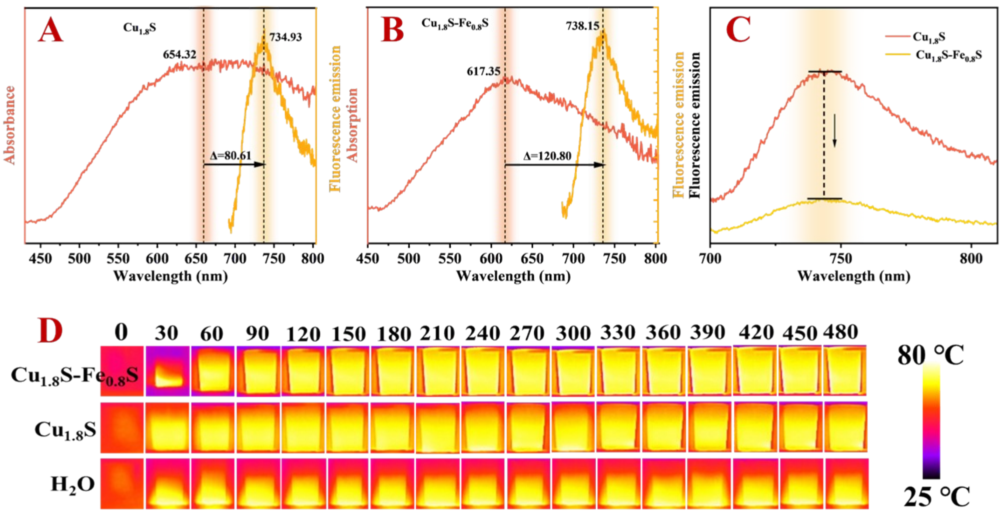

Figure S8. Stokes displacement: (A) $Cu_{1.8}S$ and (B)$Cu_{1.8}S-Fe_{0.8}S$ NPLs; (C) Fluorescence intensity comparison; (D) Heating condition of different materials.

3.4 Photothermal Immunoassay

Using the blank value as a reference, the anti-interference capability of the sensor was investigated by selecting various interfering agents, including bovine serum albumin (BSA, 100 ng/mL), immunoglobulin G (IgG, 100 ng/mL), human serum albumin (HSA, 100 ng/mL), and carcinoembryonic antigen (CEA, 80 ng/mL). The signal response decreased in the presence of individual interfering components. However, when the target analyte was mixed with these interfering substances, the signal response intensity remained consistent with that of the target alone, as illustrated in **Figure S9** (A), verifying the favorable anti-interference ability of the sensor. Reproducibility tests were then performed. Five groups of solutions with identical AFP concentrations were incubated, and the corresponding temperature responses were recorded. Each group was measured in triplicate with reassembly for each test. The results revealed that despite minor temperature fluctuations, the relative standard deviations (RSD) of these variations were all less than 4% (**Figure S9** (B)). Meanwhile, stability evaluation was conducted over a 5-week experimental period, with three parallel measurements performed at each time point. After five weeks, the temperature response only decreased by 10.7% relative to the initial value (**Figure S9** (C)). These results strongly demonstrate that the sensor exhibits satisfactory reproducibility and stability. Compared with other detection methods, this temperature-recognition system displays outstanding performance (Table S1), offering a novel potential approach for the clinical detection and therapy of tumor markers.

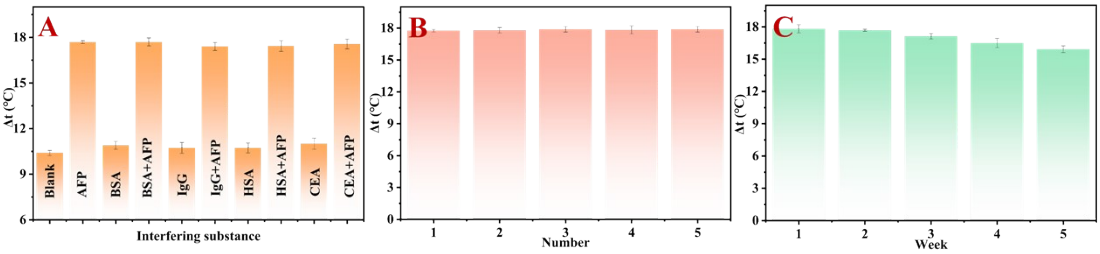

Figure S9. Sensor Performance Test: (A) Selectivity; (B) Reproducibility; (D) Stability

The blood samples were collected from Liaocheng People's Hospital. The recovery rate ranged from 97.2%-102.8%, and the relative standard deviation was less than 4%. The results of this method showed no significant difference from those of the ELISA analysis. This study has been approved by the hospital's ethics committee and complies with all applicable institutional and government regulations regarding the ethical use of human serum.

Table S1 Comparison of different methods for AFP

Analytical method	Material	Linear range (ng/mL)	Detection limit (pg/mL)	Ref.
PEC	Au-ZnO	0.05-50	18.7	□[10]
PEC	AuNPs@Zn-MOF	0.005-15	1.88	□[11]
EC	AuNPs@ZIF-8	10^{-4}-0.105	0.033	□[12]
EC	GO/NDI-1/AuNPs	10^{-5}-10	0.0033	□[13]
EC	PtNPs/MoS_2@rGO	0.001-100	0.12	□[14]
Colorimetry	GO-AgNPs	5-200	190	□[15]
FL	ZnS-CdTe	0.0004-96	10	□[16]
Photothermal	$Cu_{1.8}S$-$Fe_{0.8}S$ NPLs	0.005-100	2.6	□This work

Table S2 Determination of AFP in human serum samples

Samples (ng/mL)	Method	Added (ng/mL)	Found (ng/mL)	Recovery (%)	RSD (%)
3.26	Photothermal immunoassay	0.1	3.27±0.11	97.2	3.26
		5	8.43±0.23	102.5	2.67
		10	13.27±0.43	100.1	3.15
2.68	ELISA	0.1	2.79±0.22	100.5	2.87
		5	7.56±0.29	98.4	3.89
		10	13.04±0.36	102.8	2.76

Reference

1. Z. Li, M. Saruyama, T. Asaka and T. Teranishi, Nature Communications, 2024, 15, 4899.

2. C. Li, W. Wang, Y. Yang, S. Liu, C. Zhu and Q. Tian, CrystEngComm, 2021, 23, 6291-6299.

3.Y. Liu, M. Liu, D. Yin, L. Qiao, Z. Fu and M. T. Swihart, ACS Nano, 2018, 12, 7803-7811.

4. U. Jeong, P. H. C. Camargo, Y. H. Lee and Y. Xia, J. Mater. Chem., 2006, 16, 3893.

5. S. Jeong, J. H. Han, J.-t. Jang, J.-w. Seo, J.-G. Kim and J. Cheon, Journal of the American Chemical Society, 2011, 133, 14500-14503.

6. L. De Trizio and L. Manna, Chemical Reviews, 2016, 116, 10852-10887.

7. A. Liao, Z. Liu, Y. Wei, Q. Xie, T. Kong, M. Zeng, W. Wang, C. Yang, L. Zhang, Y. Xu, Y. Zhou and Z. Zou, Molecules,2024, 29, 3334.

8. W. Ren, Y. Yan, L. Zeng, Z. Shi, A. Gong, P. Schaaf, D. Wang, J. Zhao, B. Zou, H. Yu, G. Chen, E. M. B. Brown and A. Wu, Advanced Healthcare Materials, 2015, 4, 1526-1536.

9. W. Lai, S. Yan, M. Jiang, Z. Li, M. Wang, C. Zhao, C. Ma, Z. Wei and C. Hong, Biosensors and Bioelectronics, 2024, 252, 116151.

10. S. Xu, M. Wang, M. Chen, J. Zou, M. Zhang, L. Yu, Y. Ke, C. Zhang, H. Zhang and J. Liu, Electroanalysis, 2025, 37, e202400257.

11. X. Qin, Y. Pan, J. Zhang, J. Shen and C. Li, Talanta, 2023, 253, 123684.

12. L. Li, X. Liu, B. Su, H. Zhang, R. Li, Z. Liu, Q. Chen, T. Huang and H. Cao, Microchemical Journal, 2022, 179, 107463.

13. L.-Y. Zhao, G.-D. Shen, D.-H. Wang, W. Zhang, H.-Q. Zhao, R.-N. Ma and H.-S. Wang, Talanta, 2025, 283, 127135.

14. S. Zhang, X. Chen, S. Hu, K. Cai, C. Peng, L. Luo, Y. Gu and Y. Mei, Microchimica Acta, 2024, 191, 662.

15. L. Yang, T. Guo, B. Yao and G. Chen, Microchemical Journal, 2025, 209, 112795.

16. D. Zhu, Y. Hu, X.-J. Zhang, X.-T. Yang and Y.-Y. Tang, Microchimica Acta, 2019, 186, 124.